nature communications

Article

https://doi.org/10.1038/s41467-025-61461-2

Enhanced specific energy in fast-charging lithium-ion batteries negative electrodes via Ti-O covalency-mediated low potential

Received: 6 November 2024

Accepted: 22 June 2025

Published online: 07 July 2025

Check for updates

Jun Huang[1], Qirui Yang[1], Anyi Hu[1], Zhu Liao[1], Zhengxi Zhang[1], Qinfeng Zheng[1], Zhouhong Ren[1], Shun Zheng[1], Yixiao Zhang[1] ✉, Xiaolong Yang[2] ✉, Zhenming Xu[3], Le Zhang[4], Daming Zhu[5], Wen Wen[5], Xi Liu[1], Akihiro Orita[6], Nagahiro Saito[7], Liguang Wang[8], Yongyao Xia[3,9], Liwei Chen[1,10], Jun Lu[8] ✉ & Li Yang[1] ✉

Developing lithium-ion batteries with high specific energy and fast-charging capability requires overcoming the potential-capacity trade-off in negative electrodes. Conventional fast-charging materials (e.g., $Li_4Ti_5O_{12}$, $TiNb_2O_7$) operate at high potentials (>1.5 V vs. Li^+/Li) to circumvent lithium plating, yet this compromises specific energy. A viable strategy for enhancing the specific energy is to reduce the potential while avoiding the lithium plating risk; however, the underlying mechanisms remain unclear. Here we demonstrate that enhancing Titanium-Oxygen covalency through pseudo-Jahn-Teller Effect distortion in Ruddlesden-Popper perovskites enables low-potential operation. The $Li_2La_2Ti_3O_{10}$ negative electrode exhibits a working potential of 0.5 V vs. Li^+/Li with initial 139.3 mAh g^{-1} at 5 A g^{-1} and 72.9% capacity retention after 5000 cycles. Full cells with $LiNi_{0.8}Co_{0.1}Mn_{0.1}O_2$ positive electrodes deliver 3.45 V average discharge voltage-50% higher than conventional $Li_4Ti_5O_{12}$ || $LiNi_{0.8}Co_{0.1}Mn_{0.1}O_2$ systems-achieving 100 mAh g^{-1} at 4 A g^{-1}. Mechanistic analysis reveals low Li^+ migration barriers and stable Ruddlesden-Popper perovskite frameworks enable rapid ion transport.

The rapid advancement of lithium-ion battery applications has increased demand for power density, and specific energy, all influenced by negative electrode materials' performance[1–4]. Currently, graphite remains the most widely used negative electrode offering a high specific capacity (~375 mAh g^{-1}), excellent reversibility, and low cost[5,6]. However, its use poses a risk due to lithium dendrites formation during fast-charging at low temperatures, raised from sluggish reaction kinetics and a low operating potential (~0.1 V vs. Li^+/Li) near the lithium plating potential, which heightens the risk of short circuits[7,8]. In contrast, titanium-based intercalation materials, such as $Li_4Ti_5O_{12}$[9,10], provide a promising alternative, featuring minimal volume changes, good reversibility, and cycle stability[11]. The Ti^{4+}/Ti^{3+} redox couple has a higher working potential (~1.55 V vs. Li^+/Li), reducing dendrite formation. However, this higher potential leads to a reduced

[1]School of Chemistry and Chemical Engineering, in situ Center for Physical Sciences, Shanghai Jiao Tong University, Shanghai, China. [2]Center of Quantum Materials and Devices, College of Physics, Chongqing University, Chongqing, China. [3]College of Materials Science and Technology, Nanjing University of Aeronautics and Astronautics, Nanjing, China. [4]Department of Chemistry, The University of Texas at Austin, Austin, TX, USA. [5]Shanghai Synchrotron Radiation Facility, Shanghai Advanced Research Institute, Shanghai Institute of Applied Physics, Chinese Academy of Sciences, Shanghai, China. [6]Showa Denko Materials Co., Ltd, Tokyo, Japan. [7]Department of Chemical Systems Engineering, Nagoya University, Nagoya, Japan. [8]College of Chemical and Biological Engineering, Zhejiang University, Hangzhou, China. [9]Department of Chemistry, Fudan University, Shanghai, China. [10]i-Lab, Suzhou Institute of Nano-Tech and Nano-Bionics (SINANO), Chinese Academy of Sciences, Suzhou, China. ✉e-mail: yxzhang2019@sjtu.edu.cn; yangxl@cqu.edu.cn; junzoelu@zju.edu.cn; liyangce@sjtu.edu.cn

output voltage in full cells (2.3 V) and a low specific capacity (~175 mAh g^{-1}), thus decreasing specific energy[12].

Wadsley–Roth phases such as $TiNb_2O_7$[13] and $W_xNb_yO_z$[14] are being explored as $Li_4Ti_5O_{12}$ substitutes for their high potential (~1.65 V vs. Li^+/Li) and specific capacity (>200 mAh g^{-1}), supported by favorable Li^+ migration pathways. Research focuses on enhancing electronic/ionic conductivity, diffusion pathways, and kinetics through (1) crystal engineering (e.g., doping[15], defect/vacancy creation[16], and composite coating[17]) and (2) morphological design with nanoscale[18] and hierarchical structures[19]. These improvements enable the fast-charging negative electrode materials, and commercialization is underway, exemplified by Toshiba's next-generation super charge ion battery (SCiB), which utilizes niobium titanium oxide, due in spring 2025. Nonetheless, the specific energy remains below those of graphite-$LiFePO_4$ systems.

To further enhance specific energy, two primary strategies can be employed: increasing the specific capacity and lowering the negative electrode potential. Increasing specific capacity is constrained by the availability of lithium-ion storage sites and the efficiency of electron transfer during redox reactions. Future research should aim at developing materials capable of multi-electron transfers or incorporating reversible multi-redox centers to improve charge transfer efficiency. Lowering the negative electrode's potential is also essential to balance the lithium plating risk and higher voltages in full cell system (Fig. 1a). For example, if the lithium insertion potential of $TiNb_2O_7$ is ~ 0.5 V, Toshiba's next-generation SCiB could achieve an average voltage of about 3.3 V, 43.5% higher than the 2.3 V of existing systems. This increase could yield a specific energy, comparable to graphite-$LiFePO_4$ battery systems, while significantly improving energy density. An ideal approach would integrate both strategies, achieving a high specific capacity (>200 mAh g^{-1}) while maintaining a low operating potential to mitigate the lithium plating risk without sacrificing full battery voltage.

With low potential (<1 V) and high specific capacities (>200 mAh g^{-1}), new negative electrode materials[12,20–30] have gained significant attention. These titanium-based negative electrodes[24–31] demonstrate fast-charging capabilities and maintaining satisfactory specific energy. While Li_2TiSiO_5[24,25] and Na_2TiSiO_5[26,27] show high initial capacities, their reliance on conversion reactions, limits stability and rate performance. $Li_{0.5}La_{0.5}TiO_3$[28] has a sloping potential curve with a crossover point near 1 V, but its capacity above this potential restricts specific energy improvements. $LiYTiO_4$[29] demonstrates good electrochemical performance in bulk with multiple potential platforms (~0.3 V vs. Li^+/Li), but risks lithium plating due to significant capacity at ~0.1 V. Similarly, $K_xNa_yH_{(2-x-y)}Ti_2O_5$[30] shows a sloping potential curve (~0.8 V vs. Li^+/Li), though further rate performance improvements are needed despite its complex nanowire morphology. Despite progress, the low-potential characteristics of Ti^{4+}/Ti^{3+} redox-based materials remain underexplored, leaving a theoretical gap in developing high-energy-density, fast-charging negative electrodes. Understanding the relationship between the structure and lithium intercalation potential is critical for the rational design of advanced negative electrodes.

This study suggests that lowering the potential or enhancing the Ti^{4+}/Ti^{3+} redox energy in titanium-based oxide negative electrodes can be achieved by increasing Ti-O bond covalency. Key strategies include pseudo-Jahn–Teller effect (PJTE) distortions in TiO_6 octahedra, reducing thtanium's coordination number, or introducing low-electronegativity counter-cations to induce electron-donating effects. Lithium lathanum titanate ($Li_2La_2Ti_3O_{10}$) is examined as a model negative electrode material, demonstrating how distorted TiO_6 structures enhance Ti-O covalency via PJTE to lower the lithium intercalation potential. Without additional nanostucture design, bulk $Li_2La_2Ti_3O_{10}$ delivers a low operating potential (~0.5 V vs. Li^+/Li) with fast-charging performance, balancing fast-charging and specific energy. First-principles DFT, in situ XRD, and XAS analyses clarify its electrochemical behavior. While $Li_2La_2Ti_3O_{10}$ offers interesting electrochemical properties, $Li_2La_2Ti_3O_{10}$'s inherent limitations, such as not high initial coulombic efficiency (ICE), low specific capacity, low electronic conductivity and high manufacturing cost, show the significant gap between its current state and practical lithium-ion battery applications. But it offers valuable insights for designing next-generation high-specific-energy and fat-charging negative electrodes.

Results

Analysis of methods for lowering potential

The electrode potential (V) vs. Li^+/Li for a transition metal M, as pioneered by Goodenough et al., is determined by the position of the M^{n+1}/M^{n+} redox couple relative to the lithium Fermi energy[32]. Closer proximity of this redox energy to the lithium Fermi energy results in a lower lithium intercalation potential. Several factors influence this redox energy, including the coordination environment of the metal ion, the covalency of metal-anion bonds, the Madelung electric field, and the properties of counter cations[33]. In polyanionic positive electrode materials, increasing the coordination number of ion M, raising the electronegativity of counter-cation X, and reducing the Madelung electric field decrease the covalency of the M-O bond. This weaker covalency diminishes quantum mechanical repulsion between bonding and anti-bonding orbitals, shifting the anti-bonding orbitals away from the lithium Fermi level and increasing the potential.

Given the factors influencing positive electrode potential, increased M-O bond covalency broadens the energy gap between bonding and anti-bonding orbitals, lowering the potential vs. Li^+/Li by bringing the anti-bonding orbitals closer to the lithium Fermi level (Fig. 1b)[34]. Adjusting M-O covalency through reducing M-O coordination numbers or introducing lower-electronegativity counter-cations with electron-donating effects can raise the M^{n+1}/M^{n+} redox energy, lowering negative electrode material potential (Fig. 1c)[35]. With reduced Ti coordination in TiO polyhedra, Ti-based oxide negative electrodes, such as Li_2TiSiO_5[24,25], Na_2TiSiO_5[26,27], and $K_xNa_yH_{(2-x-y)}Ti_2O_5$[30], display low intercalation potential, with Ti in distinct TiO_5 square pyramids or TiO_4 tetrahedral structures (Fig. 1e).

As an early transition metal with low electronegativity, Ti presents challenges in enhancing Ti-O bond covalency using inductive effects. In most Ti-based oxides, Ti^{4+} typically exists in six-coordinated TiO_6 octahedra[36]. The Ti-O bond covalency is primarily determined by the molecular orbitals' energy levels formed from the Ti^{4+} 3*d* orbitals and O^{2-} 2*p* orbitals. In the TiO_6 octahedron molecular orbitals (MO) (Fig. 1f), the highest occupied molecular orbitals (HOMO) (t_{1u}, t_{2u}, t_{1g}) derive from the 2*pπ* orbitals of the six oxygen atoms, exhibiting threefold degeneracy and odd parity. Conversely, the lowest unoccupied molecular orbitals (LUMO) ($t_{2g}(3d)$: *xy*, *xz*, *yz*) predominantly consist of the dπ orbitals of the central Ti ion, also demonstrating threefold degeneracy but even parity[37].

The PJTE, first introduced in 1966[38], was used to explain the origin of ferroelectricity in the perovskite-type crystal $BaTiO_3$. The PJTE represents a fundamental mechanism in condensed matter systems, characterized by structural deformations arising from vibronic coupling—the interplay between electronic states and vibrational degrees of freedom. Distinct from the classical Jahn–Teller effect that operates in degenerate electronic configurations, the PJTE manifests in systems with non-degenerate ground states through dynamic interactions with low-energy excited states. This phenomenon is governed by electron-phonon coupling, where symmetry-breaking distortions (e.g., bond elongation/compression) are triggered to minimize the total energy of the system. Specifically, the PJTE involves a second-order perturbation mechanism that hybridizes the ground state with proximate excited states via nuclear displacements, effectively stabilizing distorted geometries even in the absence of intrinsic orbital degeneracy. By affecting the electronic structure and inducing local covalent distortions, the PJTE has significant implications in the design of advanced materials, particularly in the fields of energy storage[39], catalysis[40],

https://doi.org/10.1038/s41467-025-61461-2

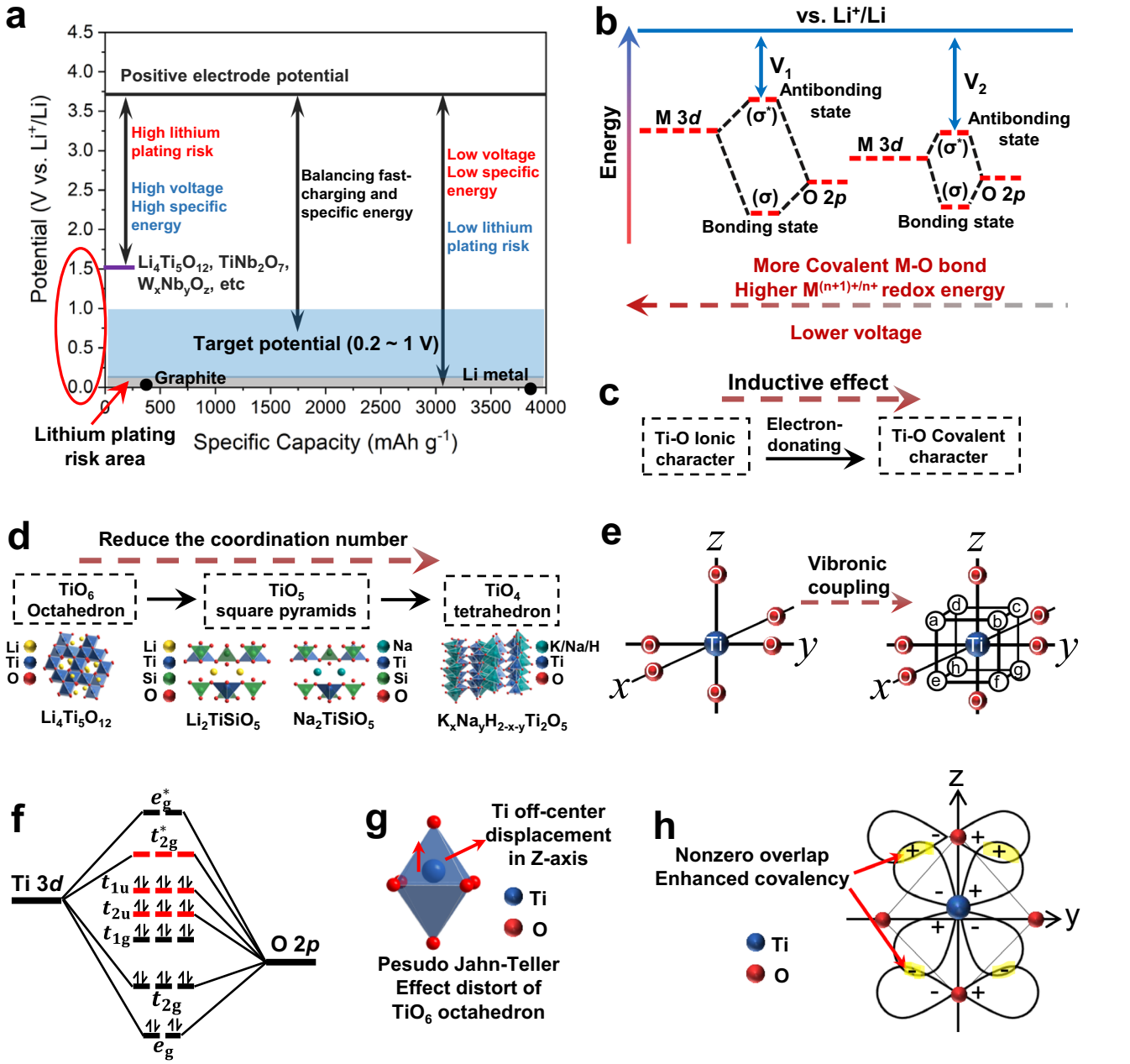

Fig. 1 | The increased specific energy of the fast-charging negative electrode material by adjusting the potential. a A helpful potential platform to balance fast-charging and specific energy. **b** The effect of M-O covalent bond strength on lithium insertion potential. The proposed method to enhance M-O covalence: **c** inductive effect and **d** decreased the coordination number. **e** The TiO_6 octahedral with Ti at the center and six O atoms at the apexes. The labels a, b, c,... represent the off-center positions of Ti in the eight wells of the adiabatic potential energy surface (APES) induced by PJTE. **f** The molecular orbital energy level diagram for the TiO_6 octahedron. Shown in red are mixed HOMO and LUMO. Illustrations to the overlap of HOMO and LUMO orbitals in TiO_6 octahedron: **g** TiO_6 octahedron with PJTE distortion of Ti off-center displacements. **h** Lifting the orthogonality between HOMO-LUMO orbitals and creating nonzero overlap resulted in enhanced covalency.

magnetism[41], and optoelectronics[42]. Taking the TiO_6 octahedron as an example, as shown in Fig. 2d, the adiabatic potential energy surface (APES) of the TiO_6 octahedron exhibits eight equivalent wells aligned along the four C_3 trigonal symmetry axes, corresponding to the off-center displacements of the Ti atom, which generate localized dipole moments[43,44].

In the regular high-symmetry TiO_6 octahedron, the HOMO-LUMO orbitals' overlap integrals are zero due to their orthogonality, meaning no contribution to Ti-O bonding, which is realized through ionic interactions or inner σ orbitals[45]. The HOMO $t_{1u}(y)$, derived from O $2p_y$ orbitals, and the LUMO formed by Ti $3d$ $t_{2g}(yz)$ orbitals are orthogonal, resulting in zero overlap as their positive and negative contributions cancel each other[46]. In contrast, in TiO_6 octahedra with PJTE distortion, as illustrated in Fig. 1g, the Ti atom off-center displacement lowers symmetry, lifting the orthogonality between HOMO-LUMO orbitals and creating nonzero overlap, thereby enhancing covalency in the Ti-O bond. Figure 1h shows that with Ti's off-center displacement in the z-direction, the overlap between HOMO $t_{1u}(y)$ and LUMO $t_{2g}(yz)$ are nonzero resulting in an additional Ti-O covalence bonding[47]. Thus, PJTE distortion in the TiO_6 octahedron enhances Ti-O bond covalency compared to the high-symmetry structure[44].

https://doi.org/10.1038/s41467-025-61461-2

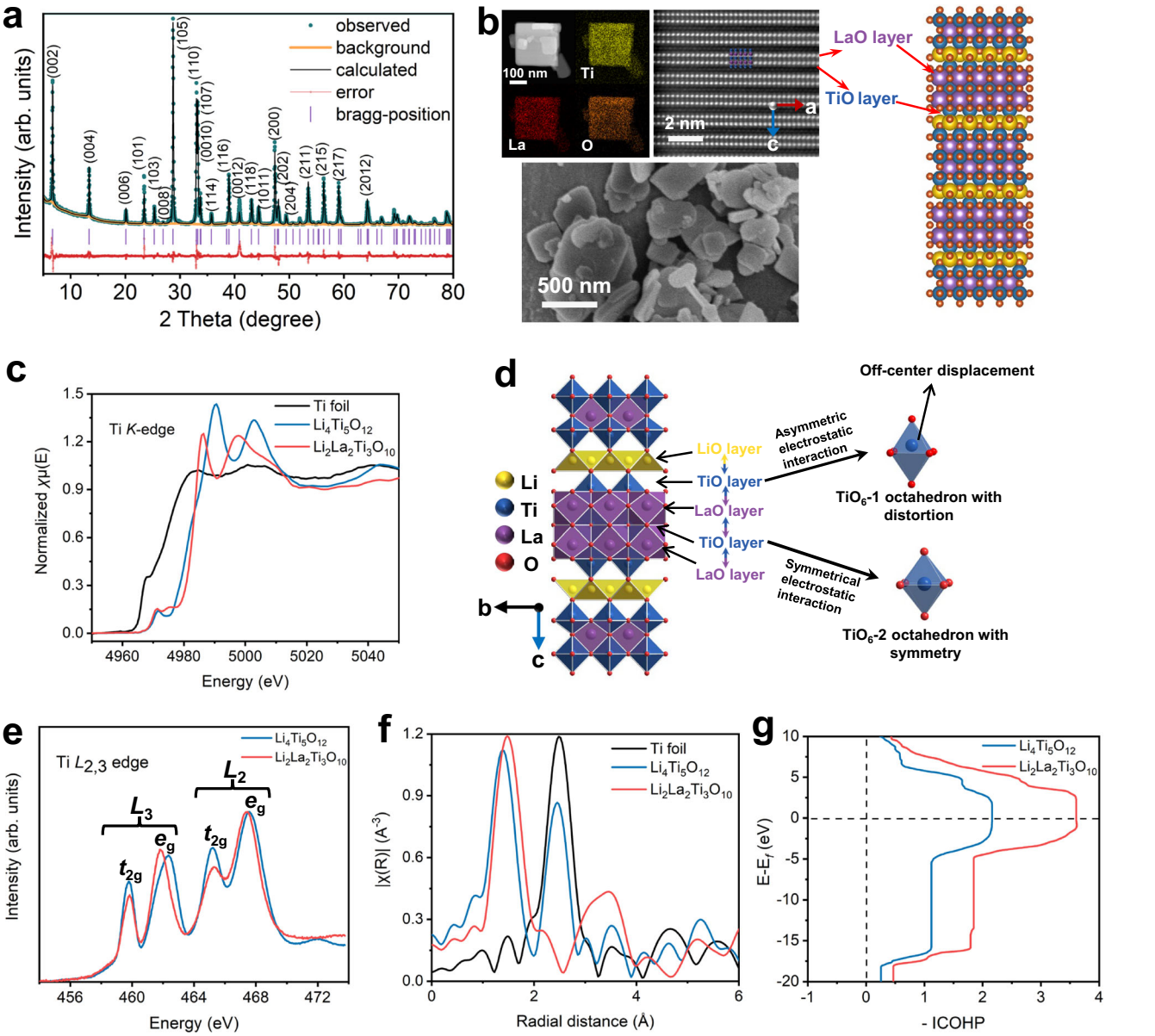

Fig. 2 | Structural characterization of $Li_2La_2Ti_3O_{10}$. **a** Rietveld refinement of $Li_2La_2Ti_3O_{10}$ powder XRD. **b** Elemental analysis including TEM image and the corresponding EDS mapping, HAADF-STEM image along the [100] direction and SEM image. **c** Ti *K*-edge XANES spectra of $Li_4Ti_5O_{12}$ and $Li_2La_2Ti_3O_{10}$. **d** Schematic of representative TiO_6-1 and TiO_6-2 octahedrons in the $Li_2La_2Ti_3O_{10}$ crystal structure schematic. **e** Ti $L_{2,3}$-edge XAS. **f** Fourier transformed R-space of Ti *K*-edge EXAFS spectra. **g** Calculated averaged integrated crystal orbital Hamiltonian population (-ICOHP) for Ti-O bond for $Li_4Ti_5O_{12}$ and $Li_2La_2Ti_3O_{10}$.

Crystal structure and characterization

The preparation of $Li_2La_2Ti_3O_{10}$ begins with synthesizing the $Na_2La_2Ti_3O_{10}$ precursor (Supplementary Fig. 1a) using the sol-gel method, followed by ion exchange with lithium nitrate. Powder X-ray diffraction (XRD) and Rietveld refinement (Fig. 2a) confirm its tetragonal crystal structure with a space group of *I4/mmm* (139) and refined cell parameters of $a = b = 3.8385(1)$ Å and $c = 26.5079(8)$ Å (Supplementary Table 1 and Supplementary Data 1)[48,49]. Energy-dispersive spectroscopic (EDS) mapping confirmed even distribution of La, Ti, and O. Atomic-resolution imaging via high-angle annular dark-field scanning transmission electron microscopy (HAADF-STEM) shows the alternating arrangement of La and Ti atoms within the perovskite-like triple unit (Fig. 2b and image processing shown in Supplementary Fig. 1b–g)[50]. The synthesized particles exhibit a flake-like morphology, with lateral dimensions of 0.5–3 µm and thicknesses ranging from 200 to 300 nm (Fig. 2b). This distinctive microstructure corresponds to relatively low specific surface area (9.561 m^2/g) and limited pore volume (0.06693 cc/g), as determined by Brunauer–Emmett–Teller (BET) and Barrett–Joyner–Halenda (BJH) analyses (Supplementary Fig. 2a and Supplementary Table 2). The Raman spectra were analyzed to identify the vibrational modes associated with its crystal structure (Supplementary Fig. 2b). The Peaks at 861.1 cm^{-1} (symmetric Ti–O stretching) and 560.7/514.4 cm^{-1} (asymmetric Ti–O stretching) confirm the distorted TiO_6 octahedra in the perovskite-like framework[51–53]. Additionally, Ti *K*-edge XANES spectra of $Li_4Ti_5O_{12}$ and $Li_2La_2T_{i3}O_{10}$ showed a shift of the absorption edge to higher energies (~4983 eV), indicating the presence of Ti in the Ti^{4+} state (Fig. 2c).

$Li_2La_2Ti_3O_{10}$ exhibits a layered Ruddlesden-Popper structure, comprising alternating alkali ion and perovskite-like layers along the c-axis. In this arrangement, Li^+ is tetrahedrally coordinated in the LiO

layer, La^{3+} is centrally positioned in the perovskite-like slabs with 12-fold coordination, and Ti^{4+} is octahedrally coordinated in the TiO layer[54,55]. Two distinct TiO_6 octahedra types are present: TiO_6-1 with PJTE distortion, found between LiO and LaO layers with asymmetric electrostatic interactions leading to off-center displacement of Ti^{4+} toward the apical oxygen, and TiO_6-2 with higher symmetry, situated between two LaO layers (Fig. 2d)[56]

To investigate structural distortions and electronic configuration, soft X-ray absorption spectroscopy (XAS) was conducted on the Ti $L_{2,3}$ edge of $Li_4Ti_5O_{12}$ and $Li_2La_2Ti_3O_{10}$, given its sensitivity to Ti coordination changes. As shown in Fig. 2e, the Ti L_3 and L_2 edges, arising from spin−orbit coupling, correspond to electronic transitions from the Ti $2p_{3/2}$ and $2p_{1/2}$ to unoccupied Ti 3*d* states near the Fermi level. Crystal field splitting further divides the L_3 and L_2 edges into two peaks, representing the e_g and t_{2g} orbitals. The t_{2g} orbitals with lower energy point toward the basal faces (d_{xy}, d_{xz}, d_{yz}) in the TiO_6 octahedron, while the e_g orbitals at higher energy point toward the apical corners ($d_{x^2-y^2}$, d_{z^2}) containing O anions.

In $Li_2La_2Ti_3O_{10}$, the Ti L_3 edge e_g peak shifts to lower energy compared to $Li_4Ti_5O_{12}$, indicating reduced crystal field splitting, and suggesting a longer average Ti-O bond length confirmed by R-space in Ti *K*-edge EXAFS (extended X-ray absorption fine structure) (Fig. 2f). The increased e_g/t_{2g} peak intensity ratio reflects lower TiO_6 octahedra symmetry in $Li_2La_2Ti_3O_{10}$. Although a larger bond length generally implies less covalency, the PJTE distortion in $Li_2La_2Ti_3O_{10}$ increases orbital overlap between Ti and O atoms, resulting in a more covalent Ti-O bond, which means the lower lithium intercalation potential[43,57]. Crystal Orbital Hamilton Population (COHP) (Supplementary Fig. 3) calculations further confirmed enhanced covalency, with the integrated COHP (-ICOHP) value for the Ti-O bond in $Li_2La_2Ti_3O_{10}$ significantly higher than in $Li_4Ti_5O_{12}$, indicating stronger covalent bonding in $Li_2La_2Ti_3O_{10}$ (Fig. 2g)[58].

Lithium-ion storage performance

Comparative analysis of galvanostatic discharge-charge profiles reveals that $Li_2La_2Ti_3O_{10}$, operates at a lower working potential (~0.5 V vs. Li^+/Li), than $Li_4Ti_5O_{12}$ (~1.55 V), despite both materials employing the Ti^{4+}/Ti^{3+} redox couple (Fig. 3a). This performance divergence originates from enhanced Ti-O bond covalency within the TiO_6 octahedra of the Ruddlesden-Popper structured $Li_2La_2Ti_3O_{10}$. When integrated with a 4 V-class positive electrode, full cells incorporating $Li_2La_2Ti_3O_{10}$ exhibit a higher average output voltage and deliver greater specific energy relative to $Li_4Ti_5O_{12}$-based counterparts.

$Li_2La_2Ti_3O_{10}$ achieves an initial discharge capacity of 430 mAh g^{-1} at 20 mA g^{-1} (Supplementary Fig. 4a), but its initial reversible charging capacity is only 260 mAh g^{-1}, leading to a low ICE of 61%. This low ICE is mainly arises from two interrelated factors: (1) the solid-electrolyte interphase (SEI) formation via electrolyte decomposition below 0.5 V (Supplementary Fig. 5a, b), (2) synthesis-induced Li^+ loss from incomplete ion exchange with Na^+ (inductively coupled plasma, ICP result in Supplementary Table 3) and H^+ incorporation during washing. This inefficiency results in irreversible consumption of Li^+, thereby increasing the manufacturing cost of LIBs. Strategies such as further optimization of synthesis protocols, electrolyte additives, and prelithiation strategies are required to bridge the gap toward industrial feasibility. Through rigorous optimization of the synthesis protocol, a direct sol-gel method that bypasses ion exchange and aqueous washing steps is successfully developed, significantly mitigating Li^+ loss and achieving an ICE of 80.77% (Supplementary Fig. 6 and Supplementary Note 1). Notably, the coulombic efficiency rapidly improves and stabilizes near 100% in subsequent cycles (Fig. 3d, c). The half cell was cycled 1000 times at various specific currents to evaluate cycling stability and rate performance. The charging specific capacity of $Li_2La_2Ti_3O_{10}$ at 2, 5, 10, and 20 A g^{-1} are 87% (195 mAh g^{-1}), 73% (164 mAh g^{-1}), 62% (139 mAh g^{-1}), and 43% (96 mAh g^{-1}) of that at 1 A g^{-1} (223 mAh g^{-1}) after activation at 100 mA g^{-1} for two cycles (Fig. 3b). Higher specific current increase polarization potential. Capacity retention over 1000 cycles at all rates exceeds 80% (Fig. 3d). Stable discharge-charge profiles (Supplementary Fig. 4b–f) confirm the reversibility and rate performance. Long-term stability is further confirmed by 5000 cycles at 5 A g^{-1} (Fig. 3e), with discharge-charge profiles maintaining consistency and a charging capacity retention of 77%, with nearly 100% coulombic efficiency.

To evaluate its potential for full cell applications, $Li_2La_2Ti_3O_{10}$ precycled (Supplementary Fig. 7a) was combined with $LiNi_{0.8}Co_{0.1}Mn_{0.1}O_2$ (NCM811), a high-energy-density positive electrode material (Supplementary Fig. 7c–e). The full cell, with a negative-to-positive electrode capacity ratio of ~1.1, exhibited a discharge capacity of 185 mAh g^{-1} at 0.1 A g^{-1} and 148 mAh g^{-1} at 1 A g^{-1} based on the mass of positive electrode active materials, with an average discharge voltage of 3.45 V (Fig. 3f), 50% higher than that of $Li_4Ti_5O_{12}$|| NCM811 full cells. To assess fast-charging capabilities and cycle stability, the full cell was tested at rates from 0.2 A g^{-1} to 4 A g^{-1}, followed by 1000 cycles at 1 A g^{-1} after activation at 0.1 A g^{-1} for the first two cycles. Discharge-charge profiles maintained similar shapes with minor polarization increases at higher rates (Fig. 3g, h). Capacity retention was 97% at 0.2 A g^{-1}, 87% at 0.4 A g^{-1}, 78% at 1 A g^{-1}, 69% at 2 A g^{-1}, and 55% at 4 A g^{-1}. After 280 cycles at 2 A g^{-1}, capacity retention exceeded 80% (Fig. 3i), and the full cell retained 74% of its initial capacity after 1000 cycles at 1 A g^{-1} (Fig. 3j). Electrochemical cycling induces the formation of robust solid-electrolyte interphase (SEI) and cathode-electrolyte interphase (CEI) layers on the $Li_2La_2Ti_3O_{10}$ and NCM811 surfaces, respectively (Supplementary Figs. 8, 9), which is crucial for enhancing the electrochemical performance and cycle stability.

High-potential fast-charging negative electrode materials such as $Li_4Ti_5O_{12}$ and $TiNb_2O_7$ face significant challenges due to unstable SEI formation and substantial gas evolution, compromising practical viability and safety. To investigate SEI stability on $Li_2La_2Ti_3O_{10}$ during lithiation, TEM (Supplementary Fig. 10 and Supplementary Note 2) and XPS (Supplementary Fig. 11 and Supplementary Note 3) analyses were conducted on electrodes at various state-of-charge (SOC) points during the first cycle and after 200 cycles under 100 mA g^{-1}. Results reveal a dynamic SEI evolution process on $Li_2La_2Ti_3O_{10}$ involving formation, partial decomposition, and eventual stabilization. Crucially, the SEI composition after the initial cycle remained largely consistent with that observed after 200 cycles, which significantly reduces interfacial impedance as evidenced by a decrease in charge-transfer resistance (R_{ct}) (Supplementary Fig. 12 and Supplementary Table 4), indicating exceptional interfacial stability. This contrasts sharply with $Li_4Ti_5O_{12}$ and $TiNb_2O_7$, where complete SEI decomposition occurs after the first charge. Differential electrochemical mass spectrometry (DEMS) (Supplementary Fig. 13) further confirmed these findings: under identical loading conditions, $Li_4Ti_5O_{12}$ exhibited much higher gas evolution than $Li_2La_2Ti_3O_{10}$ during cycling. These collective results demonstrate that the low-potential $Li_2La_2Ti_3O_{10}$ surface facilitates rapid formation of a stable SEI layer that effectively suppresses gas generation.

The electrochemical performance presented in Fig. 3 was characterized under idealized conditions featuring low active material loading (2–3 mg/cm^2) and elevated conductive carbon content (30 wt %). While this configuration isolates intrinsic material properties for fundamental evaluation, it diverges from practical battery operational requirements. To assess the practical viability of $Li_2La_2Ti_3O_{10}$, we fabricated electrodes with industrially relevant parameters (high loading >15 mg/cm^2; carbon: 5 wt%) and precycled (Supplementary Fig. 7b). Then corresponding pouch cells were assembled (Supplementary Fig. 14a), which exhibited compromised specific capacity and rate capability (Supplementary Fig. 14b–e and Supplementary Note 4). This performance deterioration is attributed to $Li_2La_2Ti_3O_{10}$'s inherently low electronic conductivity and large particle size (1–4 μm in length/width, 0.3–0.4 μm in thickness) (Supplementary Fig. 14f) resulting

https://doi.org/10.1038/s41467-025-61461-2

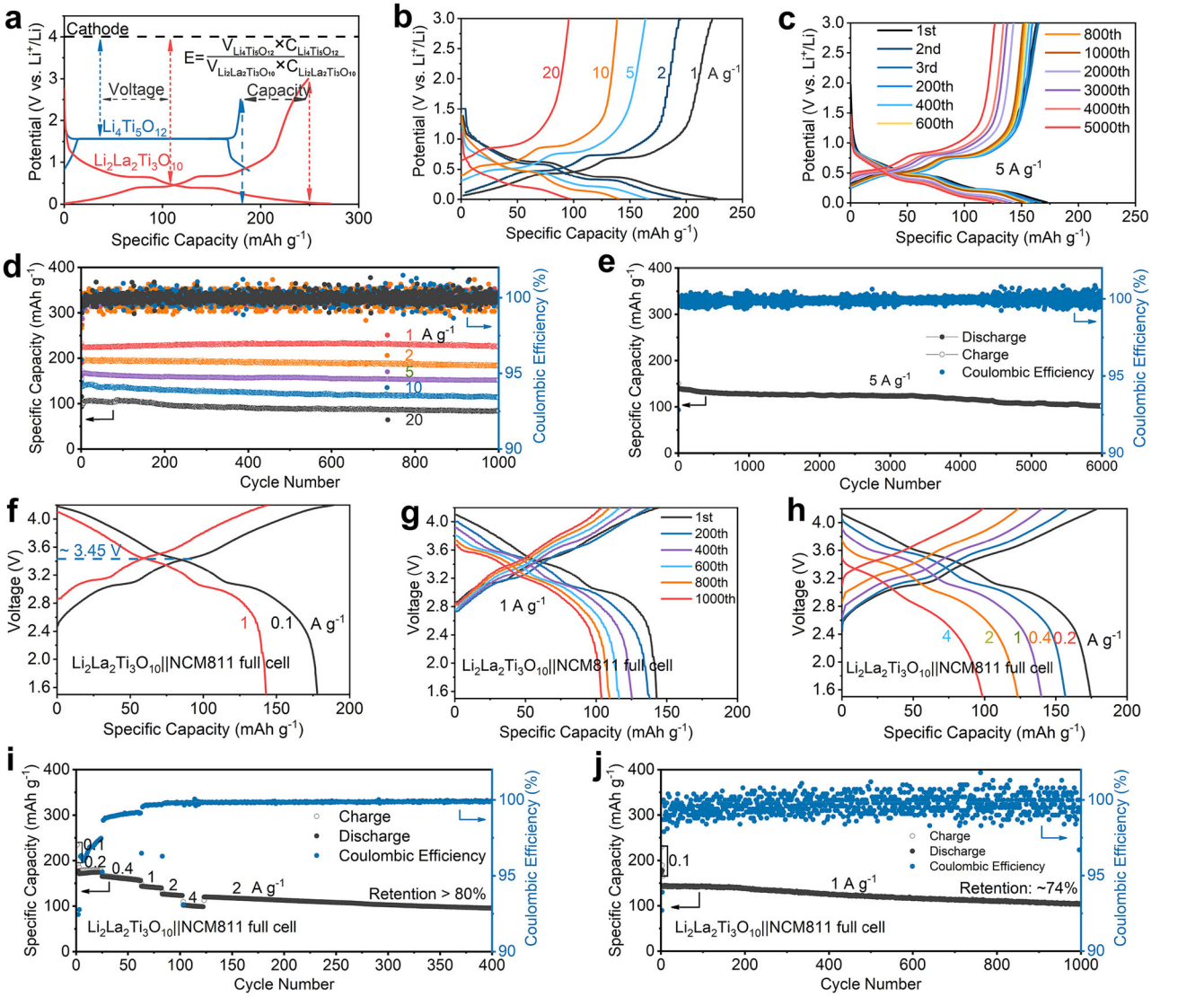

Fig. 3 | The electrochemical performance of $Li_2La_2Ti_3O_{10}$ at 25 °C. a The potential-specific capacity profiles under 20 mA g^{-1} with 0.8–2 V for $Li_4Ti_5O_{12}$ and 0.01–3 V for $Li_2La_2Ti_3O_{10}$. **b** The potential-specific capacity profiles under different specific current. **c** The potential-specific capacity profiles during 5000 cycles. **d** The cycle stability and rate performance. **e** The long-term stability under 5 A g^{-1}. **f** The voltage-specific capacity profiles of the full cell under 0.1 and 5 A g^{-1} with 1.5-4.2 V. **g** The voltage-specific capacity profiles of the full cell under various specific current. **h** The voltage-specific capacity profiles during 1000 cycles of full cell. **i** The rate performance and cycle stability of the full cell. **j** The long-term (1000 cycles) stability under 1 A g^{-1} of the full cell.

from solid-state synthesis, which collectively restricts lithium-ion diffusion kinetics under practical electrode architectures.

To decouple kinetic limitations from intrinsic material properties, we compared sol-gel synthesized $Li_2La_2Ti_3O_{10}$ (lateral dimensions: 0.3–2 µm, thickness: 0.1–0.3 µm) (Supplementary Fig. 14g) against commercial $Li_4Ti_5O_{12}$ (0.3–0.5 µm) (Supplementary Fig. 14h) under identical high-loading/low-carbon conditions. Crucially, while $Li_2La_2Ti_3O_{10}$ delivered lower specific capacities than $Li_4Ti_5O_{12}$ at low specific current (0.02–0.5 A g^{-1}), it demonstrated comparable capacities at elevated rates (Supplementary Fig. 14i). This crossover phenomenon corresponds to a higher capacity retention for $Li_2La_2Ti_3O_{10}$ versus $Li_4Ti_5O_{12}$ at 1 A g^{-1}, indicating high-rate performance despite $Li_2La_2Ti_3O_{10}$'s larger primary particle size.

Kinetics analysis and simulation calculations for fast-charging performance

First-principles calculations identified the Li^+ storage sites in the lithiated structure of $Li_2La_2Ti_3O_{10}$ (Supplementary Table 5 and Supplementary Data 2, 7). Li^+ are positioned at sites defined by four basal oxygens (O4 horizontal window), one apical oxygen, and one apical lanthanum, located above and below the LiO_4 tetrahedral layers along the c-axis (Fig. 4a). Due to electrostatic repulsion from La^{3+}, Li^+ sit above the O4 window rather than in the plane, resulting in a four-fold coordination resembling a distorted rectangular-near-planar site, characterized by frustrated coordination. The destabilization of coordination sites, relative to typical tetrahedral or octahedral Li-O coordination, reduces the energy barrier for ion hopping, thus enhancing ion mobility[59–61].

Two distinct Li^+ diffusion paths and their energy barriers were analyzed using the climbing image nudged elastic band (CINEB) and nudged elastic band (NEB) method (Supplementary Fig. 15 and Supplementary Data 3–6). The preferred path features Li^+ hopping from one O4 storage site through the O3 window to an adjacent equivalent site, with a diffusion barrier of 0.68 eV (Fig. 4b–d and Supplementary Data 3). In tetragonal $Li_2La_2Ti_3O_{10}$ ($a = b \neq c$), Li^+ diffuses in a two-dimensional plane along the a/b axes through equivalent insertion sites (Fig. 4c).

https://doi.org/10.1038/s41467-025-61461-2

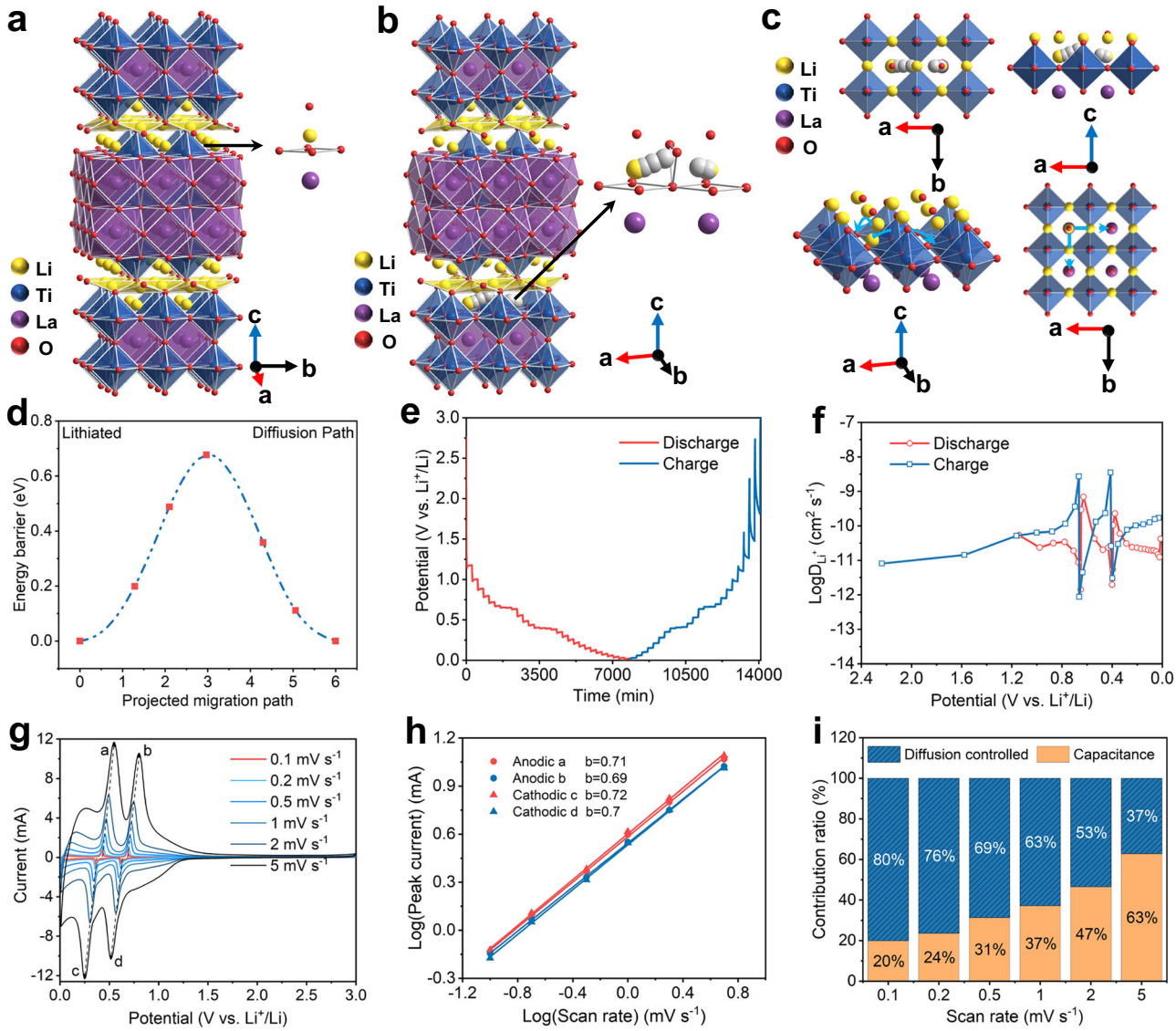

Fig. 4 | Kinetics analysis and simulation calculations. a The calculated lithiated $Li_2La_2Ti_3O_{10}$ crystal structure schematic and the magnified diagrams of Li^+ insertion site. **b** The schematic of calculated Li^+ diffusion path in lithiated $Li_2La_2Ti_3O_{10}$ and the magnified Li^+ diffusion path. **c** Viewed from c-axis and b-axis and the schematic of two-dimensional Li^+ diffusion paths. **d** Diffusion energy barrier for lithiated $Li_2La_2Ti_3O_{10}$. **e** GITT curves. **f** The lithium-ion diffusion coefficient (D_{Li^+}). **g** CV profiles at various scanning rates. **h** The calculated b values from corresponding peak currents. **i** The pseudocapacitive contribution at various scan rates.

Projected density of states (PDOS) and band gap calculations for pristine and lithiated $Li_2La_2Ti_3O_{10}$ were conducted to analyze electronic conductivity using density functional theory (DFT) (Supplementary Fig. 16). The calculated band gap for pristine $Li_2La_2Ti_3O_{10}$ is 1.93 eV, significantly narrower than that of $Li_4Ti_5O_{12}$ (3.8 eV)[62], indicating a greater likelihood of intrinsic charge carriers that facilitate faster electron compensation during rapid lithium intercalation. Upon lithiation, the PDOS reveals that the band gap vanishes, signifying a transition from semiconductor to metallic behavior, which enhances electron transfer. This transition aligns with n-type doping from lithium insertion, similar to phenomena observed in materials like $TiNb_2O_7$[63] and $Mo_{1.5}W_{1.5}Nb_{14}O_{44}$[64].

Cyclic voltammetry (CV) at various scan rates was used to analyze the kinetics of Li^+ storage. The calculated b-values for the anodic and cathodic peak currents were 0.71, 0.69, 0.72, and 0.7, respectively (Fig. 4h), indicating a mixed mechanism involving both diffusion and pseudo-capacitance (Supplementary Fig. 17), contributing to the high rate performance. To quantitatively characterize the ionic conductivity, the lithium-ion diffusion coefficient (D_{Li^+}) was measured by Galvanostatic Intermittent Titration Technique (GITT) (Fig. 4e, f), showing values between 10^{-9} and 10^{-11} $cm^2 s^{-1}$. These fast Li^+ migration kinetics ensure rapid lithium transport in $Li_2La_2Ti_3O_{10}$, further supporting its suitability for fast-charging applications.

Lithium-ion storage mechanism

To investigate the charge compensation mechanism, La L_3-edge, Ti K-edge, and O K-edge X-ray absorption spectroscopy (XAS) spectra were measured at various discharge states (pristine, 0.6, 0.35, and 0.01 V) and the charging state (3 V) (Fig. 5a–c) based on the initial discharge-charge profile (Supplementary Fig. 18a). During discharge, the La L_3-edge white line peak intensity gradually decreases (Fig. 5a), while it reappears upon charging to 3 V. This effect may result from lithium insertion, leading to the displacement of La^{3+} in the LaO polyhedral (as shown in Supplementary Fig. 19), causing electronic changes. Upon lithiation, the Ti K-edge absorption shifts to lower energy, indicating Ti reduction from +4 to +3 (Fig. 5b). Pre-edge peaks (~4970 eV), associated with covalently mixed Ti 3d and O 2p orbitals, weaken and broaden, suggesting reduced Ti-O covalency. The oxidation states of

https://doi.org/10.1038/s41467-025-61461-2

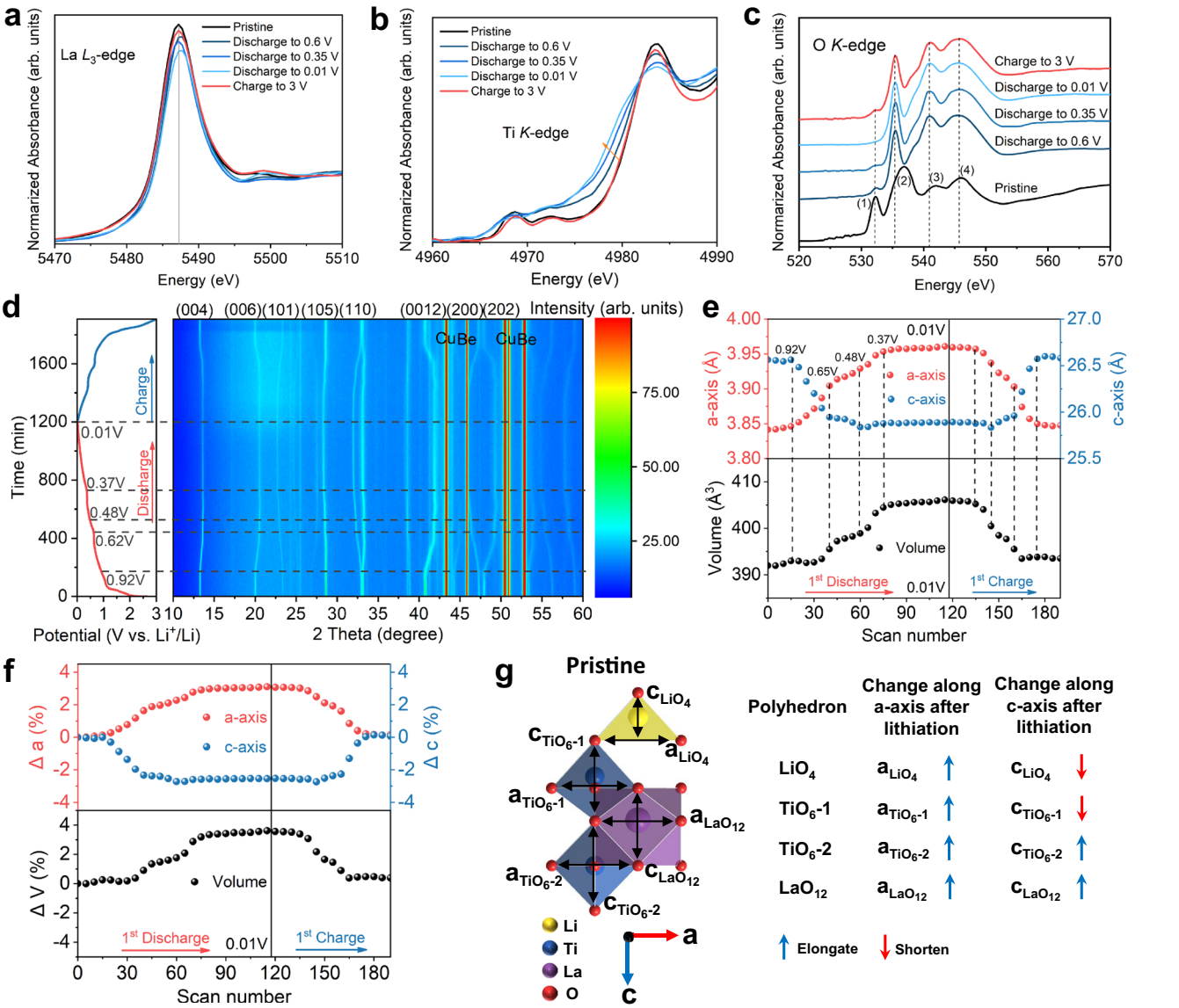

Fig. 5 | The charge compensation mechanism and structural changes of $Li_2La_2Ti_3O_{10}$. XAS of La L_3-edge (**a**), Ti *K*-edge (**b**), and O *K*-edge (**c**) under different states of charge during the first discharge-charge cycle under 20 mA g^{-1} at 25 °C. **d** Contour maps of in situ XRD during the first discharge-charge cycle under 20 mA g^{-1} at 25 °C. The change (**e**, **f**) percentage variation of the lattice parameter (a-axis, c-axis) and the unit cell volume (V) from in situ XRD. **g** The change of the width a in a-axis direction and height c in c-axis direction of polyhedrons (LiO_4, TiO_6-1, TiO_6-2, LaO_{12}) after lithiation.

La and Ti from XAS align with XPS results (Supplementary Fig. 18b, c and Supplementary Note 5). In the O *K*-edge spectra (Fig. 5c), broad peaks at 541 and 546 eV remain stable, while sharper peaks at 532 and 536 eV, linked to mixed O 2*p*–Ti 3 *d*/La 5 *d*, change: peak (1) disappears, and peak (2) sharpens, indicating altered O electronic structure. This concurrent electron transfer between O and transition metals, typical in late transition metal oxides, shows that the strong Ti-O covalency in $Li_2La_2Ti_3O_{10}$ facilitates O 2*p* electron contribution in lithiation.

To investigate structural evolution during Li^+ insertion/extraction, in situ X-ray diffraction (XRD) was conducted over two discharge-charge cycles, capturing the time-potential profile and XRD contour map from 10–60 degrees 2θ (Fig. 5d). At open-circuit potential, the diffraction peaks correspond to tetragonal-phase $Li_2La_2Ti_3O_{10}$, along with copper and beryllium peaks from the current collector and test mold. During discharge from 3 to 0.92 V, no notable diffraction peak or cell parameter changes were observed, likely due to Li^+ insertion in vacancies or pseudocapacitive storage (Fig. 5e, f). Between 0.92 and 0.37 V, diffraction peaks shift, with gradual increases in the a-axis and volume V, and a decrease in the c-axis. At 0.01 V, minimal diffraction and parameter changes indicate structural stability (Supplementary Note 6). Recharging from 0.01 V to 3 V reverses these shifts, mirroring the discharge behavior. As magnified in Supplementary Fig. 18d, e, characteristic diffraction peaks corresponding to specific crystallographic planes exhibit bidirectional shifts toward higher angles and lower angles during lithiation. This continuous peak displacement demonstrates reversible unit cell contraction/expansion during lithium-ion storage. Remarkably, the in situ XRD evolution patterns during the second discharge-charge cycle precisely replicate those observed in the initial cycle (Supplementary Fig. 20). This congruent structural response across consecutive cycles (Supplementary Fig. 21) confirms highly reversible lithium (de)intercalation mechanisms with minimal hysteresis.

To verify the reversibility of PJTE distortions in Ruddlesden-Popper structured TiO_6 octahedra, we conducted ex situ Ti $L_{2,3}$-edge

XAS on electrodes at states of charge (SOC): Pristine, Discharged to 0.5 V, Discharged to 0.01 V, and Charged to 3.0 V vs. Li^+/Li. Progressive lithium insertion to 0.01 V reduced the e_g/t_{2g} intensity ratio at the L_3-edge (Supplementary Fig. 22 and Supplementary Note 7), indicating enhanced octahedral symmetry as Ti ions migrated toward centrosymmetric positions. This aligns with DFT predictions showing decreased off-center displacement during lithiation. Subsequent charging to 3.0 V restored the e_g/t_{2g} ratio to near-pristine, confirming reversible Ti off-centering upon delithiation. Electronic localization function (ELF) (Supplementary Fig. 23) analysis reveals the distortion mechanism: In pristine $Li_2La_2Ti_3O_{10}$, asymmetric electron delocalization between Ti and apical oxygen creates stronger covalent interactions in distorted octahedra (Fig. 5b). Lithiation redistributes electron density, reducing orbital overlap and restoring symmetry. This reversible electron redistribution corroborates XAS observations, demonstrating exceptional PJTE reversibility during (de)lithiation.

Based on the above, it is evident that lithium-ion storage in $Li_2La_2Ti_3O_{10}$ follows a reversible solid-solution reaction. The corresponding chemical reaction can be expressed as: $xLi^+ + Li_2La_2Ti_3O_{10} = Li_{2+x}La_2Ti_3O_{10}$ ($2 < x < 3$). This indicates that during the charge and discharge processes, lithium ions reversibly intercalate and de-intercalate within the $Li_2La_2Ti_3O_{10}$ structure, reflecting changes in the material's composition and electronic state.

The lattice parameter changes in $Li_2La_2Ti_3O_{10}$ during lithiation are directly influenced by polyhedron size variations, reflected by bond lengths. Structural optimization calculations reveal that, upon lithiation, all polyhedrons (LiO_4, TiO_6-1, TiO_6-2, LaO_{12}) elongate along the a-axis, expanding it, while LiO_4 and TiO_6-1 shorten more along the c-axis than TiO_6-2 and LaO_{12}, compressing the c-axis (Fig. 5g and Supplementary Table 6). This aligns with in situ XRD findings, indicating a solid-solution mechanism with reversible structural changes. The maximum expansions are ~3% along the a-axis, ~2.5% shrinkage along the c-axis, and ~3.5% in unit cell volume, supporting $Li_2La_2Ti_3O_{10}$'s cycle stability and reversibility.

In summary, submicron-sized $Li_2La_2Ti_3O_{10}$ was synthesized using a sol-gel and ion-exchange method, leveraging pseudo-Jahn–Teller distortions in TiO_6 octahedra to enhance Ti–O covalency and lower lithium insertion potential. Without nanostructuring or crystallographic adjustments, bulk $Li_2La_2Ti_3O_{10}$ demonstrated low operating potential (~0.5 V vs. Li^+/Li), fast-charging (96 mAh g^{-1} at 20 A g^{-1}), and good cycle stability (72% retention after 6000 cycles at 5 A g^{-1}). When paired with NCM811, it reached a 3.45 V output, 50% higher than traditional cells, with high rate performance and stability (over 80% retention after 300 cycles at 10 C). Its fast-charging is attributed to low energy barriers, two-dimensional Li^+ diffusion channels, and minimal volume change (~3.5%), all supporting its cycle stability. These findings underscore PJTE-induced covalency as a promising strategy for developing advanced, high-performance battery electrodes.

Methods

Synthesis of $Li_2La_2Ti_3O_{10}$

First, $Na_2La_2Ti_3O_{10}$ was synthesized by the sol-gel method, and then ion-exchanged with molten $LiNO_3$ to obtain $Li_2La_2Ti_3O_{10}$. In a typical process, at room temperature, 0.0045 mol titanium metal powder (Ti, 99.99%, Aladdin) and 5 mL aqueous ammonia ($NH_3{\cdot}H_2O$, 25.0–28.0%, Sinopharm Chemical Reagent) were added successively to 15 mL hydrogen peroxide aqueous solution (H_2O_2, 30%, Sinopharm Chemical Reagent), stirring continuously until a uniform and transparent yellow solution A was formed. 0.027 mol citric acid monohydrate ($C_6H_8O_7{\cdot}H_2O$, AR, Sinopharm Chemical Reagent) was added to solution A and stirred to form titanium chelate citric acid. 0.003 mol lanthanum nitrate hexahydrate ($La(NO_3)_3{\cdot}6H_2O$, 99.99%, Aladdin), 0.006 mol sodium hydroxide (NaOH, AR, Sinopharm Chemical Reagent) and 0.006 mol nitric acid (HNO_3, 65–68%, Sinopharm Chemical Reagent) were sequentially added to 15 mL deionized water and stirred until all dissolved to form a transparent solution B. Under stirring, solution B was added dropwise to solution A to form a transparent red mixed solution, which was further stirred for 30 min. After dropping nitric acid or aqueous ammonia to maintain the pH of the mixed solution at 5–6, continue to stir for 30 min. Then, 0.027 mol of ethylene glycol ($C_2H_6O_2$, AR, Sinopharm Chemical Reagent) was added to the mixed solution. After being stirred for 30 min, the mixed solution was placed in a 60 °C oven for 1 h, and then heated at 90 °C for 1 h, and then heated at 140 °C for 10 h to evaporate and dry. After that, a fluffy metal citric acid complex solid was obtained, and then it was ground into powder in a mortar and put into a corundum crucible. After heat treatment of the metal citric acid complex powder (heating to 350 °C at a rate of 3–4 °C per minute in the heating furnace for 1 h, then heating to 900 °C at a rate of 3–4 °C per minute for 2 h, and then cooling naturally to room temperature), the $Na_2La_2Ti_3O_{13}$ white powder was obtained.

After mixing the $Na_2La_2Ti_3O_{13}$ white powder with 0.006 mol lithium nitrate ($LiNO_3$, 99.9%, Aladdin), the mixed powder was ground evenly. After the mixed powder was heated at 350 °C for 20 h, the obtained product was collected and ground evenly. Then it was washed three times with deionized water and ethanol, respectively, and then dried in a 100 °C oven for 12 h to obtain $Li_2La_2Ti_3O_{13}$ white powder.

Preparation of electrodes

The single-side coated $Li_2La_2Ti_3O_{13}$ electrodes for coin cell were prepared by mixing 60 wt% active material with 30 wt% carbon black (Super P Li, TIMCAL) and 10 wt% carboxymethylcellulose sodium (CMC-Na, Aladdin) to form a slurry with deionized water as solvent, which was coated onto a copper foil (15-μm thick, MTI) and dried at 70 °C for 30 min. Then the copper foil coated with dried slurry was cut into electrodes with a diameter of 12 mm by a manual slicing machine (MSK-T10, MTI). The electrodes were dried under vacuum at 120 °C for 12 h. The loading of active materials for electrodes was >2 mg cm^{-2}.

The $LiNi_{0.8}Co_{0.1}Mn_{0.1}O_2$ (NCM811) electrodes were prepared with 80 wt% active material, 10 wt% carbon black (Super P Li, TIMCAL) and 10 wt% poly (vinylidene difluoride) (PVDF, HSV 900, ARKEMA). The slurry prepared by mixing $LiNi_{0.8}Co_{0.1}Mn_{0.1}O_2$ (MTI), carbon black and poly (vinylidene difluoride) with 1-methyl-2-pyrrolidinone (C_5H_9NO, anhydrous, 99.5%, Aladdin) in an argon-filled glovebox (H_2O < 0.1 ppm, O_2 < 0.1 ppm, Mbraun) was coated onto an aluminum foil (20-μm thick, MTI) and dried at 70 °C for 30 min. Then the aluminum foil coated with dried slurry was cut into electrodes with a diameter of 12 mm by a manual slicing machine. The electrodes were dried under vacuum at 120 °C for 12 h. The loading of active materials for electrodes was >2 mg cm^{-2}. Prior to full cell assembly, the $Li_2La_2Ti_3O_{10}$ negative electrode was precycled in a Li-metal half cell for one cycle under 20 mA g^{-1} and two cycles under 100 mA g^{-1} with 0.01–3 V cutoff potentials at 25 °C to form a stabilized SEI. This effectively compensated for the irreversible Li^+ loss, eliminating the need for excess positive electrode capacity. This extra pre-treatment step, while essential for optimizing the material's properties, could contribute to higher manufacturing costs.

The fabrication of pouch cells

The pouch cells were fabricated with technical support from the National Engineering Research Center for Nanotechnology and Application.

Positive electrode preparation. Commercial $LiNi_{0.6}Co_{0.2}Mn_{0.2}O_2$ (NCM622) positive electrodes (Shenzhen Kejing) were employed in pouch cell fabrication. Electrodes featured 16-μm-aluminum foil current collectors with two configurations: Single-sided coating: areal loading = 11 ± 0.2 mg/cm^2 (active material). Double-sided coating: areal loading = 22 ± 0.4 mg/cm^2. Coating dimensions measured 10 × 6 cm with active material comprising 97.5 wt% of the composite. The reference specific capacity was 170 mAh g^{-1} at 0.1 C (3.0–4.3 V vs. Li^+/Li).

Negative electrode preparation. $Li_2La_2Ti_3O_{10}$ negative electrodes were formulated with 90 wt% active material, 5 wt% carbon black (Super P Li, TIMCAL), and 5 wt% poly(vinylidene difluoride) binder (PVDF, HSV 900, Arkema). Coatings (10.2 × 6.2 cm) achieved an areal loading of 20 ± 0.4 mg cm^{-2} per side on copper foil (15 µm). All electrodes underwent vacuum drying at 120 °C for 10 h before argon-glovebox transfer.

Single-layer pouch cells containing one double-sided $Li_2La_2Ti_3O_{10}$ anode and two Li-metal foils (100-µm thickness, 10.5 × 6.5 cm) were precycled under 20 mA g^{-1} for two cycles at 25 °C. Pre-cycled negative electrodes were extracted in an argon glovebox and reconstituted into multilayer stacks comprising: 5 × double-sided LLTO anodes, 4 × double-sided NCM622 cathodes, 2 × single-sided NCM622 cathodes. Separators (Celgard 2500) and electrolyte (1.0 M LiPF6 in EC: EMC:DMC 1:1:1) were used, and electrolyte filling: 1.5 mL and 5 mL electrolyte volumes were used for single-layer and Ah-level pouches, respectively. All cells underwent electrochemical testing under uniform external pressure (0.8 MPa) applied via screw-clamped fixtures.

Electrochemical measurements

The lithium metal||$Li_2La_2Ti_3O_{10}$ half cells were assembled using CR2016 coin cells in an argon-filled glovebox (H_2O < 0.1 ppm, O_2 < 0.1 ppm, Mbraun) with the lithium-metal foil (1.2-mm thick, 14-mm diameter) as the counter electrode and the glass microfiber filters (GF/A, Whatman) as the separator. Before assembling the half cell, the surface of the lithium-metal foils was cleaned with a banister brush. The electrolyte was 1.0 M $LiPF_6$ in 1:1 v/v ethylene carbonate (EC) and dimethyl carbonate (DMC), and the volume is 100 µL.

The lithium metal||$LiNi_{0.8}Co_{0.1}Mn_{0.1}O_2$ half cells and $Li_2La_2Ti_3O_{10}$||$LiNi_{0.8}Co_{0.1}Mn_{0.1}O_2$ full cells were also assembled using CR2016 coin cells in an argon-filled glovebox. A Celgard 2500 membrane (the number: 1, thickness: 25-µm, lateral dimension: d = 19 mm, porosity: 55% and average pore size: 0.064 µm) was employed as the separator and the electrolyte was 1.0 M $LiPF_6$ dissolved in a solvent of ethylene carbonate (EC)/ethyl methyl carbonate (EMC)/dimethyl carbonate (DMC) (1:1:1 v/v/v) and the volume is 100 µL.

After the cells were assembled, the electrochemical measurements were performed after standing for 8 h to ensure sufficient infiltration between the electrolyte and the electrode. The galvanostatic charge/discharge measurements were carried on the LAND cell test system (CT3002A and CT2001A, Wuhan SHENGLAN, China) in the potential range of 0.01–3 V for the lithium metal||$Li_2La_2Ti_3O_{10}$ half cells and 3–4.3 V for the lithium metal||$LiNi_{0.8}Co_{0.1}Mn_{0.1}O_2$ half cells and 1.5–4.2 V for the $Li_2La_2Ti_3O_{10}$||$LiNi_{0.8}Co_{0.1}Mn_{0.1}O_2$ full cells at 25 ± 2 °C.

Cyclic voltammetry tests and electrochemical impedance spectroscopy (EIS) are performed on an electrochemical workstation (CHI660E, CHENHUA), and the same half cell is tested at least three times at a certain scan rate to ensure data reliability. Electrochemical impedance spectroscopy (EIS) measurements were conducted in potentiostatic mode using a sinusoidal alternating voltage perturbation with an amplitude of 5 mV RMS (0.005 V). The frequency range spanned from 0.1 Hz to 100 kHz (10^5 Hz), with 12 logarithmically spaced points per decade and 1 averaging cycle per frequency point. Prior to each frequency sweep, the system was stabilized at the open-circuit potential (OCP) for 2 s (quiet time). The data of galvanostatic intermittent titration technique (GITT) measurements were collected at a specific current of 20 mA g^{-1} for 30 min and a stand interval of 4 h.

Structural characterizations

The powder X-ray diffraction was conducted on a Bruker D8 Advance diffractometer with Cu Kα radiation in the 2θ range of 5–80°. The morphology and microstructure of samples were observed by a field emission scanning electron microscope (Nova NanoSEM 450, FEI). The energy-dispersive X-ray spectroscopy (EDS) mapping and scanning transmission electron microscopy (STEM) with the annular dark-field (ADF) and the high-angle annular dark-field (HAADF) images were performed using Hitachi HF5000 and FEI Themis Z spherical aberration-corrected transmission electron microscopes (200 KeV).

X-ray photoelectron spectroscopy (XPS) experiments were carried out on a NEXSA (Thermo Fisher Scientific) spectrometer. For XPS measurements, by disassembling the lithium metal||$Li_2La_2Ti_3O_{10}$ cells in a glovebox, the electrode samples in different discharge-charge states were obtained, and after being washed three times with DMC and dried, the electrode samples were sent to an XPS spectrometer for testing through the vacuum sample transfer, avoiding exposure to air. All the XPS peaks were calibrated according to the C–C bond peak at 284.6 eV. (It is worth noting that due to the existence of SEI film on the electrode surface, it is difficult to observe the valence state of elements in different states of charge by XPS. However, here we collect the signal of the electrode near the current collector side, which is not affected by SEI, and can be considered as the signal of the electrode bulk phase, and the data is more reliable.)

The in situ XRD experiments were performed on a Bruker D8 Advance diffractometer with Cu Kα radiation (λ = 1.5406 Å) in the reflection mode. The XRD spectrums were collected in the 2θ range of 10–60° every ten minutes. The in situ test battery was a customized battery model with a Be window through which X-rays can be transmitted. The customized battery model could consist of a 14 mm diameter electrode (35 mm diameter current collector), 19 mm diameter separator and lithium-metal foil (0.6 mm thick, 16 mm diameter) to form a half cell. The $Li_2La_2Ti_3O_{10}$ electrode for in situ XRD experiment were prepared by mixing 60 wt% active material with 30 wt% carbon black (Super P Li, TIMCAL) and 10 wt% Carboxymethylcellulose sodium (CMC-Na, Aladdin) to form a slurry with deionized water as solvent, which was coated onto the center of a 35 mm diameter copper mesh foil collector (9-µm thick with 1.5 mm pore size, MTI) and dried at 70 °C for 30 min. The electrodes were dried under vacuum at 120 °C for 12 h. The loading of active materials for electrodes was 5–6 mg cm^{-2}. The in situ half cell was assembled in an argon-filled glovebox (H_2O < 0.1 ppm, O_2 < 0.1 ppm, MIKROUNA) with the glass microfiber filters (GF/A, Whatman) as the separator. The electrolyte was 1.0 M $LiPF_6$ in 1:1 v/v ethylene carbonate (EC) and dimethyl carbonate (DMC). During the in situ XRD experiments, the customized in situ test battery was cycled for two cycles in the potential range of 0.01–3 V at a specific current of 20 mA g^{-1}. The change of lattice parameters (including a-axis, c-axis and unit cell volume V) (Fig. 5e, f) were obtained according to in situ XRD structure refinement software from the Bruker company, which are also consistent with the results obtained from Bragg's law (Supplementary Figs. 11, 12).

The X-ray absorption fine structure (XAFS) of the Ti *K*-edges and La L_3-edges were collected in transmission mode using ion chamber detectors with a Si(111) double-crystal monochromator (room temperature) at beamline BL14W1 of the Shanghai Synchrotron Radiation Facility (SSRF). The Soft X-ray absorption spectroscopy (sXAS) of the O *K*-edges and Ti $L_{2,3}$-edges were obtained at the beamline BL02B of SSRF using bulk-sensitive total fluorescence yield (TFY) and surface-sensitive total electron yield (TEY) modes. The incident photon energy was calibrated before data collection in all measurements. The XAFS data were performed using Athena software[65].

All ex situ samples of batteries with various states of charge were disassembled in an argon-filled glovebox. Following disassembly, the electrodes were immersed in anhydrous dimethyl carbonate (DMC) for 2 h to remove residual electrolytes, subsequently dried in the glovebox, and finally encapsulated using either polyimide tape or an inert transfer holder for further characterization.

Computational methods

All calculations were carried out in the framework of the density functional theory (DFT) calculations, which were implemented in the Vienna ab initio simulation package (VASP) software[66], within the Perdew–Burke–Ernzerh of generalized gradient approximation (GGA)

for the exchange-correlation functional[67]. Core electrons and the nuclei were treated by the projector augmented wave method, and the plane-wave energy cutoff was set to 550 eV. The lattice parameters and internal atomic positions were fully relaxed until the total energy and maximum ionic Hellmann-Feynman force were less than 10^{-10} eV and 10^{-4} eV/Å, respectively. The projected density of states (PDOS) of pristine and lithiated $Li_2La_2Ti_3O_{10}$ were computed within a Monkhorst −Pack grid of 24 × 24 × 3 k-points. To characterize the strength of the Ti-O interaction, the Crystal Orbital Hamilton Population (COHP) were computed by the Lobster program[68], in which the negative and positive COHP values indicate bonding and anti-bonding, respectively, and the electron localization function (ELF) visualized by the VESTA tool[69]. The climbing image nudged elastic band (CINEB) and nudged elastic band (NEB) method was utilized to calculate the minimum energy paths (MEPs) of Li ion migration. To verify the reliability of our results, we also performed CINEB and NEB calculations[70]. The threshold for the total force acting on the CINEB and NEB images was set to 0.03 eV/Å, and the energy convergence criterion of 10^{-5} eV was used.

Cyclic voltammetry (CV) with different scan rates and galvanostatic intermittent titration technique (GITT)

The first three CV curves of $Li_2La_2Ti_3O_{10}$ negative electrode in the range of 3 to 0.01 V at a scan rate of 0.1 mV s^{-1} (Supplementary Fig. 7a), are well overlapped, indicating good lithium-ion storage reversibility, except for the wide cathodic peak of the first cycle due to the formation of SEI film. Two couples of redox peaks at 0.43 V/0.37 V and 0.69 V/0.62 V with very low potential hysteresis (<0.1 V), correspond to the redox couples of Ti^{4+}/Ti^{3+}, respectively.

The CV curves at different scan rates from 0.1 to 5 mV s^{-1} are shown in Fig. 4g. With the increase of scan rate, the cathodic reduction peaks and anodic oxidation peaks become wider due to the increase of polarization. The relationship between the scan rate (v) and the response current (i) under a certain potential (V) as follows:

$$i_{(V)} = av^b \tag{1}$$

$$\log i_{(V)} = b \log v + \log a \tag{2}$$

where the b value obtained by calculating the slope of the log$i_{(V)}$ - log$v$ plot depends on the mechanism of ion storage. Specifically, a b value of 0.5 means the complete diffusion control mechanism, while a b value of 1 means a capacitive contribution, including surface pseudocapacitive effect from charge transfer with surface or subsurface atoms or a non-Faraday contribution mechanism of the electric double-layer effect.

The capacitance contribution can be quantitatively determined by dividing the response current (i) at a certain potential (V) into two parts: capacitance (represented by $k_{1(V)}v$) and diffusion control reaction (marked as $k_{2(V)}v^{1/2}$), as shown below:

$$i_{(V)} = k_{1(V)}v + k_{2(V)}v^{1/2} \tag{3}$$

$$i_{(V)}/v^{1/2} = k_{1(V)}v^{1/2} + k_2 \tag{4}$$

where both $k_{1(V)}$ and $k_{2(V)}$ obtained by calculating from the $i_{(V)}/v^{1/2}$-$v^{1/2}$ plot are constants for a certain potential (V). k_1 is the slope, while k_2 is the y-axis intercept.

Based on Ficks second law, the lithium-ion diffusion coefficient can be calculated by the following formula:

$$D_{Li^+} = \frac{4}{\pi\tau}\left(\frac{m_B V_M}{M_B S}\right)^2 \left(\frac{\Delta E_S}{\Delta E_t}\right)^2 \ldots\ldots\ldots (\tau << L^2/D_{Li^+}) \tag{5}$$

Where τ is the pulse time of constant current, m_B is the mass of the active material, V_M is the material molar volume, M_B is the material molar mass, S is the surface area of electrode, ΔE_s is the difference between the two equilibrium potentials, and ΔE_t is the potential change of the coin cell for a constant current for the time τ.

Data availability

All data that support the findings of this study are presented in the manuscript and Supplementary Information. Source data are provided with this paper.

References

1. Liu, Y. Y., Zhu, Y. Y. & Cui, Y. Challenges and opportunities towards fast-charging battery materials. *Nat. Energy* **4**, 540–550 (2019).
2. Wang, C. Y. et al. Fast charging of energy-dense lithium-ion batteries. *Nature* **611**, 485–490 (2022).
3. Armand, M. & Tarascon, J. M. Building better batteries. *Nature* **451**, 652–657 (2008).
4. Jin, H. C. et al. Black phosphorus composites with engineered interfaces for high-rate high-capacity lithium storage. *Science* **370**, 192–197 (2020).
5. Zhao, L. et al. Revisiting the roles of natural graphite in ongoing lithium-ion batteries. *Adv. Mater.* **34**, 2106704 (2022).
6. Zhang, H., Yang, Y., Ren, D. S., Wang, L. & He, X. M. Graphite as anode materials: fundamental mechanism, recent progress and advances. *Energy Storage Mater.* **36**, 147–170 (2021).
7. Zhang, Y. et al. Search for stable host materials as low-voltage anodes for lithium-ion batteries: a mini-review. *Energy Storage Mater.* **55**, 364–387 (2023).
8. Holoubek, J. et al. Exploiting mechanistic solvation kinetics for dual-graphite batteries with high power output at extremely low temperature. *Angew. Chem.-Int. Ed.* **58**, 18892–18897 (2019).
9. Liu, H. D. et al. Elucidating the limit of Li insertion into the spinel $Li_4Ti_5O_{12}$. *ACS Mater. Lett.* **1**, 96–102 (2019).
10. Thackeray, M. M. & Amine, K. $Li_4Ti_5O_{12}$ spinel anodes. *Nat. Energy* **6**, 683–683 (2021).
11. Zhang, W. et al. Kinetic pathways of ionic transport in fast-charging lithium titanate. *Science* **367**, 1030–1034 (2020).
12. Liu, H. D. et al. A disordered rock salt anode for fast-charging lithium-ion batteries. *Nature* **585**, 63–67 (2020).
13. Shi, A. R. et al. Highly oxidized state dopant induced Nb-O bond distortion of $TiNb_2O_7$ for extremely fast-charging batteries. *Nano Energy* **123**, 109349 (2024).
14. Griffith, K. J., Wiaderek, K. M., Cibin, G., Marbella, L. E. & Grey, C. P. Niobium tungsten oxides for high-rate lithium-ion energy storage. *Nature* **559**, 556–563 (2018).
15. Zhang, Y. et al. Delocalized electronic engineering of $TiNb_2O_7$ enables low temperature capability for high-areal-capacity lithium-ion batteries. *Nat. Commun.* **15**, 6299 (2024).
16. Voskanyan, A. A., Jayanthi, K. & Navrotsky, A. Vacancy control in $TiNb_2O_7$: implications for energy applications. *Chem. Mater.* **34**, 10311–10319 (2022).
17. Gong, S. Y. et al. Self-assembly $TiNb_2O_7$@MXene anode material for fast and stable lithium storage. *Energy Fuels* **37**, 3159–3165 (2023).
18. Zhang, X. L. et al. Design, perspective, and challenge of niobium-based anode materials for high-energy alkali metal-ion batteries. *Adv. Funct. Mater.* **34**, 2405392 (2024).
19. Yang, C. F. et al. Crystallographic insight of reduced kattice volume expansion in mesoporous Cu^{2+}-doped $TiNb_2O_7$ microspheres during Li^+ insertion. *Adv. Funct. Mater.* **33**, 2212854 (2023).
20. Wang, R. et al. Fast-charging" mechanism of Li_3VO_4 from the perspective of material science for lithium-ion battery. *Chem. Eng. J.* **498**, 155371 (2024).

21. Ma, Y. J. et al. Introducing highly redox-active atomic centers into insertion-type electrodes for lithium-ion batteries. *Adv. Energy Mater.* **10**, 2000783 (2020).
22. Yang, L. T. et al. A new sodium calcium cyclotetravanadate framework: "zero-strain" during large-capacity lithium intercalation. *Adv. Funct. Mater.* **32**, 2105026 (2022).
23. Zhang, Q. et al. Zero-strain" $K_2SrV_4O_{12}$ as a high-temperature friendly Li^+-storage material. *Energy Storage Mater.* **52**, 637–645 (2022).
24. Liu, J. Y. et al. Li_2TiSiO_5: a low potential and large capacity Ti-based anode material for Li-ion batteries. *Energy Environ. Sci.* **10**, 1456–1464 (2017).
25. He, D. et al. TiO_2 nanocrystal-framed Li_2TiSiO_5 platelets for low-voltage lithium battery anode. *Adv. Funct. Mater.* **30**, 2001909 (2020).
26. Zhang, Y. et al. Low-potential and high-capacity lithium battery anode based on hierarchical assemblies of Na_2TiSiO_5 nanotubes. *Appl Surf. Sci.* **604**, 154409 (2022).
27. Zhao, S., He, D., Wu, T. H., Wang, L. H. & Yu, H. J. Ultrastable orthorhombic Na_2TiSiO_5 anode for lithium-ion battery. *Adv. Energy Mater.* **12**, 2102709 (2022).
28. Zhang, L. et al. Lithium lanthanum titanate perovskite as an anode for lithium ion batteries. *Nat. Commun.* **11**, 3490 (2020).
29. Zhang, Y. et al. Layered perovskite lithium yttrium titanate as a low-potential and ultrahigh-rate anode for lithium-ion batteries. *Adv. Energy Mater.* **12**, 2200922 (2022).
30. Yuan, C. H. et al. $K_xNa_yH_{(2-x-y)}Ti_2O_5$ for high-performance lithium-ion battery anode with Li dendrites-free mechanism, zero-strain characteristic. *Adv. Energy Mater.* **13**, 2302015 (2023).
31. Huang, J., Yang, K. H., Zhang, Z. X., Yang, L. & Hirano, S. I. Layered perovskite $LiEuTiO_4$ as a 0.8 V lithium intercalation electrode. *Chem. Commun.* **53**, 7800–7803 (2017).
32. Goodenough, J. B. & Kim, Y. Challenges for rechargeable Li batteries. *Chem. Mater.* **22**, 587–603 (2010).
33. Gutierrez, A., Benedek, N. A. & Manthiram, A. Crystal-chemical guide for understanding redox energy variations of $M^{2+/3+}$ couples in polyanion cathodes for lithium-Ion batteries. *Chem. Mater.* **25**, 4010–4016 (2013).
34. Melot, B. C. & Tarascon, J. M. Design and preparation of materials for advanced electrochemical storage. *Acc. Chem. Res* **46**, 1226–1238 (2013).
35. Kuznetsov, D. A. et al. Tuning redox transitions via inductive effect in metal oxides and complexes, and implications in oxygen electrocatalysis. *Joule* **2**, 225–244 (2018).
36. Wang, D. et al. Fundamentals and advances of ligand field theory in understanding structure-electrochemical property relationship of intercalation-type electrode materials for rechargeable batteries. *Prog. Mater. Sci.* **133**, 101055 (2023).
37. Bersuker, I. B. Spontaneous symmetry breaking in matter induced by degeneracies and pseudodegeneracies. *Adv. Chem. Phys.* **160**, 159–208 (2016).
38. Bersuker, I. B. On origin of ferroelectricity in perovskite-type crystals. *Phys. Lett.* **20**, 589–590 (1966).
39. Zhang, J. L. et al. Regulating pseudo-Jahn-Teller effect and superstructure in layered cathode materials for reversible alkali-ion intercalation. *J. Am. Chem. Soc.* **144**, 7929–7938 (2022).
40. Xia, B. K., Du, J. L., Li, M., Duan, J. J. & Chen, S. Pseudo-Jahn-Teller effect breaks the pH dependence in two-electron oxygen electroreduction. *Adv. Mater.* **36**, 2401641 (2024).
41. Liu, H. M. & Khaliullin, G. Pseudo-Jahn-Teller effect and magnetoelastic coupling in spin-orbit mott insulators. *Phys. Rev. Lett.* **122**, 057203 (2019).
42. Rao, M. et al. Strain coupling and Jahn-Teller effect in efficient and stable sky-blue germanium-lead perovskites. *J. Mater. Chem. C***10**, 6827–6836 (2022).
43. Bersuker, I. B. Pseudo-Jahn-Teller effect-a two-state paradigm in formation, deformation, and transformation of molecular systems and solids. *Chem. Rev.* **113**, 1351–1390 (2013).
44. Polinger, V. & Bersuker, I. B. Pseudo Jahn-Teller effect in permittivity of ferroelectric perovskites. *J. Phys. Conf. Ser.* **833**, 012012 (2017).
45. Polinger, V., Garcia-Fernandez, P. & Bersuker, I. B. Pseudo Jahn-Teller origin of ferroelectric instability in BaTiO type perovskites: the Green's function approach and beyond. *Phys. B* **457**, 296–309 (2015).
46. Bersuker, I. B. Vibronic (pseudo Jahn-Teller) theory of ferroelectricity: novel aspects and applications. *Ferroelectrics* **536**, 1–59 (2018).
47. Bersuker, I. B. Jahn-Teller and pseudo-Jahn-Teller effects: from particular features to general tools in exploring molecular and solid state properties. *Chem. Rev.* **121**, 1463–1512 (2021).
48. Toda, K., Watanabe, J. & Sato, M. Crystal structure determination of ion-exchangeable layered perovskite compounds, $K_2La_2Ti_3O_{10}$ and $Li_2La_2Ti_3O_{10}$. *Mater. Res. Bull.* **31**, 1427–1435 (1996).
49. Zhang, B. H. et al. Hybrid improper ferroelectricity in A-site cation ordered $Li_2La_2Ti_3O_{10}$ ceramic with triple-layer Ruddlesden-Popper structure. *Appl. Phys. Lett.* **118**, 052903 (2021).
50. Wang, Y. J. et al. Hole trapping process and highly sensitive ratiometric thermometry over a wide temperature range in Pr^{3+}-doped $Na_2La_2Ti_3O_{10}$ layered perovskite microcrystals. *J. Phys. Chem. A* **123**, 4021–4033 (2019).
51. Blasse, G. & van den Heuvel, G. P. M. Vibrational spectra and structural considerations of compounds NaLnTiO4. *J. Solid State Chem.* **10**, 206–210 (1974).
52. Byeon, S. H., Lee, S. O. & Kim, H. Structure and raman spectra of layered titanium oxides. *J. Solid State Chem.* **130**, 110–116 (1997).
53. Nozaki, R. et al. Vibrational study of layered perovskites $M_2La_2Ti_3O_{10}$ (M = Li, Na, K, Rb): Raman spectra and normal mode analysis. *J. Phys. Chem. B* **105**, 7950–7953 (2001).
54. Gustin, L. et al. From tetrahedral to octahedral Iron coordination: Layer compression in topochemically prepared $FeLa_2Ti_3O_{10}$. *Inorg. Chem.* **55**, 11529–11537 (2016).
55. Fanah, S. J. & Ramezanipour, F. Strategies for enhancing lithium-ion conductivity of triple-layered Ruddlesden-Popper oxides: case study of $Li_{2-x}La_{2-y}Ti_{3-z}Nb_zO_{10}$. *Inorg. Chem.* **59**, 9718–9727 (2020).
56. Borstnar, P. et al. Transient Ruddlesden-Popper-type defects and their influence on grain growth and properties of lithium lanthanum titanate solid electrolyte. *ACS Nano* **18**, 10850–10862 (2024).
57. Bersuker, I. B. A local approach to solid state problems: pseudo Jahn-Teller origin of ferroelectricity and multiferroicity. *J. Phys Conf. Ser.* **428**, 012028 (2013).
58. Li, Y. et al. Localized vibration and avoided crossing in $SrTi_{11}O_{20}$ for oxide thermoelectrics with intrinsically low thermal conductivity. *J. Mater. Chem. A* **9**, 11674–11682 (2021).
59. McColl, K. & Cora, F. Fast lithium-ion conductivity in the 'empty-perovskite' n=2 Ruddlesden-Popper-type oxysulphide $Y_2Ti_2S_2O_5$. *J. Mater. Chem. A* **9**, 7068–7084 (2021).
60. Rong, Z. Q. et al. Materials design rules for multivalent Ion mobility in intercalation structures. *Chem. Mater.* **27**, 6016–6021 (2015).
61. Horrocks, G. A. et al. Mitigating cation diffusion limitations and intercalation-induced framework transitions in a 1D tunnel-structured polymorph of V_2O_5. *Chem. Mater.* **29**, 10386–10397 (2017).
62. Chiu, H. C. et al. Capacity fade mechanism of $Li_4Ti_5O_{12}$ nanosheet anode. *Adv. Energy Mater.* **7**, 1601825 (2017).
63. Griffith, K. J. et al. Ionic and electronic conduction in $TiNb_2O_7$. *J. Am. Chem. Soc.* **141**, 16706–16725 (2019).
64. Tao, R. M. et al. Insight into the fast-rechargeability of a novel $Mo_{1.5}W_{1.5}Nb_{14}O_{44}$ anode material for high-performance lithium-ion batteries. *Adv. Energy Mater.* **12**, 2200519 (2022).

65. Ravel, B. & Newville, M. ATHENA, ARTEMIS, HEPHAESTUS: data analysis for X-ray absorption spectroscopy using IFEFFIT. *J. Synchrotron Rad.* **12**, 537–541 (2005).
66. Kresse, G. & Furthmuller, J. Efficient iterative schemes for ab initio total-energy calculations using a plane-wave basis set. *Phys. Rev. B* **54**, 11169–11186 (1996).
67. Perdew, J. P., Burke, K. & Ernzerhof, M. Generalized gradient approximation made simple. *Phys. Rev. Lett.* **77**, 3865–3868 (1996).
68. Maintz, S., Deringer, V. L., Tchougreeff, A. L. & Dronskowski, R. LOBSTER: a tool to extract chemical bonding from plane-wave based DFT. *J. Comput. Chem.* **37**, 1030–1035 (2016).
69. Momma, K. & Izumi, F. VESTA: a three-dimensional visualization system for electronic and structural analysis. *J. Appl. Crystallogr* **41**, 653–658 (2008).
70. Henkelman, G., Uberuaga, B. P. & Jonsson, H. A climbing image nudged elastic band method for finding saddle points and minimum energy paths. *J. Chem. Phys.* **113**, 9901–9904 (2000).

Acknowledgements

The authors gratefully acknowledge funding supported by the National Key Research and Development Program (Grant No. 2019YFE0122500, L.Y.), the National Natural Science Foundation of China (Grant No. 22178216, L.Y.), Natural Science Foundation of Shanghai (No. 21ZR1434800, Z.Z.). The authors are grateful to the Instrumental Analysis Center of Shanghai Jiao Tong University for material characterizations. This work was partially supported by the High Performance Computing Platform of Nanjing University of Aeronautics and Astronautics.

Author contributions

J.H., Z.Z., L.Y., and J.L. conceived and designed this work. J.H., Y.Z., Q.Z., and L.C. conducted in situ XRD testing. X.L., Z.R., and L.C. perform the HADDF characterization. X.Y., Z.X., and Y.X. did the DFT calculations. J.H., D.Z., and W.W. analyzed in situ XRD data. J.H., Z.L., A.H., Q.Y., S.Z., L.W., and L.Z. processed and analyzed the XPS and XAFS data. L.Y., L.C., L.W., A.O., N.S., and J.L. guided writing and data analysis. J.H. drafted the manuscript, and all authors were involved in revising the manuscript.

Competing interests

The authors declare no competing interests

Additional information

Supplementary information The online version contains supplementary material available at https://doi.org/10.1038/s41467-025-61461-2.

Correspondence and requests for materials should be addressed to Yixiao Zhang, Xiaolong Yang, Jun Lu or Li Yang.

Peer review information *Nature Communications* thanks Isaak Bersuker, and the other, anonymous, reviewer(s) for their contribution to the peer review of this work. A peer review file is available.